An Optical–Thermal Surface–Atmosphere Radiative Transfer Model Coupling Framework With Topographic Effects

Hanyu Shi, *Student Member, IEEE*, Zhiqiang Xiao, *Member, IEEE*, Jianguang Wen, *Member, IEEE*, and Shengbiao Wu

***Abstract*— Most surface–atmosphere radiative transfer models (RTMs) work only for flat surfaces, with the exception being time-consuming 3-D scene-based models. The deficiency of flat-surface RTMs that do not consider topographic effects is that their applications in earth observation and simulation studies are impaired because rugged terrains make up approximately 24% of the global land surface. Another deficiency of most surface–atmosphere RTMs is that they model reflected and emitted (i.e., solar and thermal) radiative transfer processes separately, which limits RTMs in applications, such as fire detection. This study proposes a unified optical–thermal RTM coupling framework (RTM-CF) that considers topographic effects based on the four-stream approximation theory. The framework couples surface–atmosphere RTMs and can simultaneously simulate a set of parameters at the top-of-atmosphere (TOA) and bottom-of-atmosphere (BOA) levels from optical and thermal spectral ranges. These parameters include the TOA directional radiance/reflectance, TOA exitance/albedo, TOA net radiation, surface radiance/reflectance/albedo, surface downward/upward/net radiation, and FAPAR/APAR. The RTM-CF with topographic effects is compared with the well-known 3-D discrete anisotropic radiative transfer (DART) ray-tracing model and validated by field measurements from three steep sites. The evaluation results show that the simulated reflectance, radiance, and radiation fluxes are consistent with the DART results and the field data, with $R^2 > 0.93$ and scatter points close to the 1:1 line for all parameters. In this RTM-CF, atmospheric and topographic effects are simultaneously incorporated, and the surface anisotropy is also effectively considered. This framework is highly modularized, which enables it to be easily adapted to different submodels.**

***Index Terms*— Leaf angle distribution (LAD), optical–thermal, radiative transfer, surface radiation, topography.**

I. Introduction

LAND surface parameters, such as the leaf area index (LAI), surface albedo, fraction of absorbed photosynthetically active radiation (FAPAR), and surface temperature, are traditionally estimated from the reflectance or radiance of the surface, the accuracy of which determines the accuracy of the estimated parameters. Both the topographic effect and the atmospheric effect should be corrected to obtain accurate surface reflectance/radiance. In most studies, topographic and atmospheric corrections are conducted separately [1]. However, the two effects are indeed coupled, and the physical models are often required for simultaneously correcting the combined atmospheric and topographic effects to obtain accurate estimates of the reflectance or radiance of the surface [1]–[11]. The crucial point about these simultaneous correction methods is that they build coupled surface–atmosphere radiative transfer models (RTMs) to describe the interactions between the atmosphere and the terrain surface accurately. Three important aspects are involved: 1) the distribution of the downwelling radiation; 2) the reflective/emissive properties of the surface; and 3) the interactions between radiation and the surface. The characterizations of the first two terms usually determine the third term.

Currently, 3-D RTMs, which typically adopt Monte Carlo or ray-tracing methods, are the most accurate models for surface–atmosphere RTM coupling [12]–[14]. However, 3-D models are very complicated and computationally expensive and are, thus, difficult to use for parameter inversion. Therefore, many simplification strategies have been developed. For example, the assumption of a 1-D plane-parallel atmosphere is used by many successful atmospheric RTMs, such as MODerate resolution atmospheric TRANsmission (MODTRAN), libRadtran, second simulation of the satellite signal in the solar spectrum (6S), and Santa Barbara DISORT atmospheric radiative transfer (SBDART). Another example is dividing the incident solar radiation (ISR) into direct and isotropic diffuse parts at the bottom-of-atmosphere (BOA), and this method is commonly adopted by surface–atmosphere RTM coupling methods [15]–[24]. In addition, single- and multiple-scattering radiances are often modeled separately [16], [17], [22], [25], [26]. However, except for 3-D scene-based RTMs, such as the discrete anisotropic radiative transfer (DART), the underlying surfaces are all assumed to be flat in the above RTMs, which are not able to simulate topographic effects.

The topographic effect is a factor that must inevitably be considered when processing remote sensing data, especially high spatial resolution data. Topography affects both surface downwelling and upward radiation, thus altering the balance

Manuscript received October 10, 2020; revised November 16, 2020; accepted December 6, 2020. This work was supported by the National Natural Science Foundation of China under Grant 41771359. *(Corresponding author: Zhiqiang Xiao.)*

Hanyu Shi and Zhiqiang Xiao are with the State Key Laboratory of Remote Sensing Science, Faculty of Geographical Science, Beijing Normal University, Beijing 100875, China (e-mail: shihanyu@mail.bnu.edu.cn; zhqxiao@bnu.edu.cn).

Jianguang Wen is with the State Key Laboratory of Remote Sensing Science, Aerospace Information Research Institute, Chinese Academy of Sciences, Beijing 100101, China (e-mail: wenjg@radi.ac.cn).

Shengbiao Wu is with the School of Biological Sciences, The University of Hong Kong, Hong Kong (e-mail: shengwu@hku.hk).

This article has supplementary material provided by the authors and color versions of one or more figures available at https://doi.org/10.1109/TGRS.2020.3044061.

Digital Object Identifier 10.1109/TGRS.2020.3044061

of surface energy; it also affects solar–surface–sensor geometries, thus changing the observed radiance. Wen *et al.* [27] analyzed the effects of topography on the land surface bidirectional reflectance distribution function (BRDF) and found that topography could greatly influence its shape and magnitude. The influences of topographic effects on surface short- and long-wave radiations have also been demonstrated in many studies [28]–[33]. For example, Chen *et al.* [28] found that the errors induced by ignoring topography were 5–20 W/m^2 in general circulation models with smoothed topography. Yan *et al.* [30], [32] found that the error induced by neglecting topographic effects exceeded 100 W/m^2 for the long-wave net flux at the Tibetan Plateau and the Heihe watershed. Wang *et al.* [33] found that it is necessary to consider topographic effects on surface solar radiation even when using moderate-resolution remotely sensed data, such as the Moderate Resolution Imaging Spectroradiometer (MODIS) data and the Advanced Very High Resolution Radiometer (AVHRR) data. In addition, ignoring topography induces errors in the retrieval of surface parameters, such as LAI, FAPAR, land cover, surface albedo, and surface temperature [34]–[40].

Although many studies have analyzed the influences of topography in forward modeling and parameter inversion, they only focus on specific parameters that ignore physical connections among different parameters. This connection is very important when the parameters serve as input to drive models, such as land process models and climate models [41], [42]. The influences of topography on the optical and thermal bands are independently modeled. Many optical (thermal) remote-sensing studies ignore the thermal (solar) contributions, but the solar and thermal signals are of equal importance at specific spectrum ranges, such as the range from 3 to 5 μm, which is very important for surface fire detection [43], [44]. In addition, modeling solar and thermal radiative transfers separately results in errors in the estimation of certain parameters, such as surface net radiation (SNR) [45], [46]. Therefore, a unified optical–thermal RTM with topographic effects is needed.

In this study, a unified optical–thermal RTM coupling framework (RTM-CF) with topographic effects is developed. This framework incorporates atmospheric and topographic effects simultaneously, and a set of parameters can be simulated from it. For example, the parameters at the top-of-atmosphere (TOA) level include TOA directional radiance/reflectance, TOA exitance/albedo, and TOA net radiation and the parameters at the BOA level include the surface radiance/reflectance/albedo, surface downward/upward/net radiation, and FAPAR/APAR. Details of the proposed RTM-CF are given in Section II, where four validation schemes (VSs) are also presented. Section III presents the validation of this RTM-CF, and the discussion and conclusion are provided in Sections IV and V, respectively.

II. Methodology

A. Unified Optical–Thermal RTM-CF With Topographic Effects

The four-stream approximation theory [15], [19] is used to couple the surface and atmospheric RTMs, and a brief introduction to the necessary background information is given here. Imagine a medium layer above an underlying surface, as shown in Fig. 1. The reflectance matrix at the top of this coupled scene R_s^* can be expressed as follows [15]:

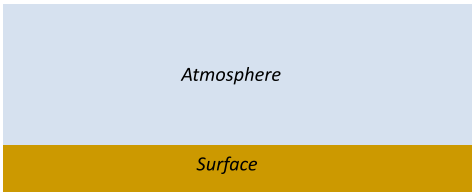

Fig. 1. Schematic of the surface–atmosphere system.

$$R_s^* = \begin{bmatrix} r_{sd}^* & r_{dd}^* \\ r_{so}^* & r_{do}^* \end{bmatrix} = R_t + T_u(I - R_s R_b)^{-1} R_s T_d \tag{1}$$

where R_s is the reflectance matrix of the underlying surface, R_b is the reflectance matrix for the bottom of the medium layer, and R_t is the reflectance matrix for the top surface of the isolated medium layer. T_d and T_u are the transmittance matrices for the incoming and outgoing radiation (direct and diffuse), respectively, and I is the identity matrix

$$R_s = \begin{bmatrix} r_{sd} & r_{dd} \\ r_{so} & r_{do} \end{bmatrix}, \quad R_t = \begin{bmatrix} \rho_{sd} & \rho_{dd} \\ \rho_{so} & \rho_{do} \end{bmatrix}, \quad R_b = \begin{bmatrix} 0 & 0 \\ \rho_{dd}^b & 0 \end{bmatrix}$$
$$T_d = \begin{bmatrix} \tau_{ss} & 0 \\ \tau_{sd} & \tau_{dd} \end{bmatrix}, \quad T_u = \begin{bmatrix} \tau_{dd} & 0 \\ \tau_{do} & \tau_{oo} \end{bmatrix} \tag{2}$$

where r indicates the reflection above the underlying surface or the ensemble system, ρ is the inner reflection of the medium layer, and τ is the transmission through the medium layer. The subscript "s" represents the direct flux in the solar direction, the subscript "d" represents the hemispherical diffuse flux, the superscript "b" represents bottom of the atmosphere, and the subscript "o" indicates the radiance (times π) in the direction of observation. Table I gives detailed explanations of the matrix elements [19].

By applying (1), a coupled surface–atmosphere RTM can be established. In the following text, the superscript "A" is associated with atmospheric variables, while the superscript "L" indicates surface variables.

1) TOA Modeling: The TOA reflectance matrix $\overline{R}_s^A$ (a variable with an overline indicates that it is for flat surfaces only; this distinguishes between it and variables for terrain surfaces) over a flat surface [15], [47] is

$$\overline{R}_s^A = R_t^A + T_u^A \left(I - \overline{R}_s^L R_b^A\right)^{-1} \overline{R}_s^L T_d^A \tag{3}$$

where the term $(I - \overline{R}_s^L R_b^A)^{-1}$ denotes the multiple-reflection process between the atmosphere and the surface. In particular, the element $\overline{r}_{so}^A$ in $\overline{R}_s^A$ is the TOA bidirectional reflectance factor (BRF) of a flat surface–atmosphere system

$$\overline{r}_{so}^A = \rho_{so}^A + \tau_{ss}^A \overline{r}_{so}^L \tau_{oo}^A + \frac{\left(\tau_{ss}^A \overline{r}_{sd}^L + \tau_{sd}^A \overline{r}_{dd}^L\right)\tau_{do}^A}{1 - \overline{r}_{dd}^L \rho_{dd}^{A\_b}} + \frac{\left(\tau_{sd}^A + \tau_{ss}^A \overline{r}_{sd}^L \rho_{dd}^{A\_b}\right)\overline{r}_{do}^L \tau_{oo}^A}{1 - \overline{r}_{dd}^L \rho_{dd}^{A\_b}}. \tag{4}$$

As expressed in (3), the multiple-reflection process works at the intersection plane of the atmosphere and the surface,

TABLE I
TRANSMITTANCE AND REFLECTANCE MATRIX ELEMENTS

r_{so}, r^*_{so}	Bi-directional reflectance factor of surface and ensemble system
r_{sd}, r^*_{sd}	Directional-hemispherical reflectance of surface and ensemble system
r_{do}, r^*_{do}	Hemispherical-directional reflectance factor of surface and ensemble system
r_{dd}, r^*_{dd}	Bi-hemispherical reflectance of surface and ensemble system
ρ_{so}	Bi-directional reflectance of medium (for black underlying surfaces)
ρ_{sd}	Directional-hemispherical reflectance of medium (for black underlying surfaces)
ρ_{do}	Hemispherical-directional reflectance of medium (for black underlying surfaces)
ρ_{dd}	Bi-hemispherical reflectance of medium (for black underlying surfaces)
ρ^b_{dd}	Bi-hemispherical reflectance of medium at the bottom, or spherical albedo of medium
τ_{ss}, τ_{oo}	Direct transmittance of medium in incident and observation direction
τ_{sd}	Directional-hemispherical transmittance of medium in incident direction
τ_{do}	Hemispherical-directional transmittance of medium in observation direction
τ_{dd}	Bi-hemispherical transmittance of medium

which is horizontal. For a sloping surface, in this study, the multiple-reflection process is still modeled at the intersection of the atmosphere and the surface, but it is now a sloping plane. The modeling of this process over a slope can be achieved by rotating the underlying surface. Consider a terrain surface with a slope β and an aspect φ_T. The TOA reflectance matrix over the terrain is modeled as

$$R^A_s = R^A_t + T^A_u P^{\text{out}}_T \left(I - R^L_s R^A_b\right)^{-1} R^L_s P^{in}_T T^A_d \tag{5}$$

where

$$P^{in}_T = \begin{bmatrix} F_{\text{sun}} & 0 \\ 0 & F_{\text{sky}} \end{bmatrix}, \quad P^{\text{out}}_T = \begin{bmatrix} V_{\text{sky}} & 0 \\ 0 & 1 \end{bmatrix} \tag{6}$$

are the terrain matrices. F_{sun} and F_{sky} [34] are

$$F_{\text{sun}} = \zeta \frac{\cos\theta_{is}}{\cos\theta_s}; \quad F_{\text{sky}} = k\frac{\cos\theta_{is}}{\cos\theta_s} + (1-k)V_{\text{sky}} \tag{7}$$

where θ_s and φ_s are the solar zenith and azimuth angles, respectively. Furthermore, $\cos\theta_{is} = \cos\theta_s\cos\beta + \sin\theta_s\sin\beta\cos(\varphi_s - \varphi_T)$, where ζ is a binary factor (0 or 1) that indicates whether the pixel is self-shadowed or shielded by other pixels [48], [49]. θ_{is} is the intrinsic solar zenith angle that refers to the sloping surface. V_{sky} is the sky view factor, defined as the relative proportion of the solid angle of the sky [49]. F_{sky} considers both the isotropic and anisotropic circumsolar diffuse irradiances, and k is the proportion of anisotropic components to total diffuse irradiance. k can be replaced by τ^A_{ss} in practical use [34], [50]. This terrain algorithm considers the topographic effects on direct solar radiation and the obstruction of the surrounding topography for hemispherical radiation. There are several different algorithms to calculate V_{sky}, and the intercomparison among them can be found in [51]. The most widely used method in the remote-sensing community is probably the one developed by Dozier and Frew [49]

$$V_{\text{sky}} = \frac{1}{\pi}\int_0^{2\pi}\int_0^{H_\phi} \eta_d(\theta,\varphi)\sin\theta[\cos\theta\cos\beta + \sin\theta\sin\beta \times \cos(\varphi - \varphi_T)]d\theta d\varphi \tag{8}$$

where H_φ is the horizon angle. $\eta_d(\theta,\varphi)$ is the anisotropic factor, and its value is equal to 1 for isotropic radiation

$$V_{\text{sky}} = \frac{1}{2\pi}\int_0^{2\pi}[\cos\beta\sin^2 H_\varphi + \sin\beta\cos(\varphi - \varphi_T) \times (H_\varphi - \sin H_\varphi\cos H_\varphi)]d\varphi. \tag{9}$$

The discretization of (9) is

$$V_{\text{sky}} = \frac{1}{N}\sum_{i=1}^{N}[\cos\beta\sin^2 H_{\varphi_i} + \sin\beta\cos(\varphi_i - \varphi_T) \times (H_{\varphi_i} - \sin H_{\varphi_i}\cos H_{\varphi_i})] \tag{10}$$

where N is the number of discretized azimuth angle φ_i, and H_{φ_i} is the horizon angle in direction i. Previous studies showed that $N = 64$ is accurately enough [34], and it is adopted in this study. It can be seen from (10) that the digital elevation model (DEM) data are needed to calculate V_{sky} accurately. When DEM is not available or involved, the approximation method proposed by Liu and Jordan [52] can be used, which is $V_{\text{sky}} = (1 + \cos\beta)/2$.

Similarly, the element r^A_{so} in R^A_s is the TOA BRF for a sloping surface

$$\begin{aligned} r^A_{so} = {} & \rho^A_{so} + \tau^A_{oo} r^L_{so} F_{\text{sun}} \tau^A_{ss} \\ & + \frac{\tau^A_{do} V_{\text{sky}}\left(r^L_{sd} F_{\text{sun}} \tau^A_{ss} + r^L_{dd} F_{\text{sky}} \tau^A_{sd}\right)}{1 - r^L_{dd}\rho^{A\_b}_{dd}} \\ & + \frac{\tau^A_{oo} r^L_{do}\left(F_{\text{sky}}\tau^A_{sd} + \rho^{A\_b}_{dd} r^L_{sd} F_{\text{sun}}\tau^A_{ss}\right)}{1 - r^L_{dd}\rho^{A\_b}_{dd}} \end{aligned} \tag{11}$$

and the element r^A_{sd} is the TOA hemispherical-directional reflectance factor (HDRF) (also TOA albedo)

$$r^A_{sd} = \rho^A_{sd} + \frac{\tau^A_{dd} V_{\text{sky}}\left(r^L_{sd} F_{\text{sun}}\tau^A_{ss} + r^L_{dd} F_{\text{sky}}\tau^A_{sd}\right)}{1 - r^L_{dd}\rho^{A\_b}_{dd}}. \tag{12}$$

The TOA upward radiation flux matrix E^A_u can be calculated from the TOA downward radiation flux matrix E^A_d

$$E^A_u = R^A_s E^A_d \tag{13}$$

and

$$\begin{aligned} E^A_d &= \begin{bmatrix} E^A_s\cos\theta_s & 0 \end{bmatrix}^T \\ E^A_u &= \begin{bmatrix} E^A_+ & E^A_o \end{bmatrix}^T \end{aligned} \tag{14}$$

where E_s^A is the monochromatic extra-terrestrial solar irradiance on a plane perpendicular to the sunrays at the TOA, and θ_s is the solar zenith angle. E_o^A is the flux-equivalent radiance in the view direction, and E_+^A is the upward radiation flux at the TOA.

At this point, the TOA reflective properties over the terrain surface are developed through (5)–(14). However, the development process is only suitable for the short-wave spectrum range where the thermal radiation is negligible. When considering thermal radiation, the TOA upward flux matrix E_u^A becomes

$$E_u^A = R_s^A E_d^A + J_u^A \tag{15}$$

and

$$J_u^A = J_t^A + T_u^A P_T^{\text{out}} \left(I - J_s^L R_b^A\right)^{-1} J_s^L Q_T J_d^A \tag{16}$$

In (16), J_u^A, J_t^A, J_s^L, Q_T^{in}, and J_d^L are

$$\begin{aligned} J_u^A &= \begin{bmatrix} J_+^A & J_o^A \end{bmatrix}^T, \quad J_t^A = \begin{bmatrix} j_+^A & j_o^A \end{bmatrix}^T, \quad J_d^A = \begin{bmatrix} 1 & j_-^A \end{bmatrix}^T \\ J_s^L &= \begin{bmatrix} j_+^L & r_{dd}^L \\ \zeta j_o^L & r_{do}^L \end{bmatrix}, \quad Q_T = \begin{bmatrix} 1 & 0 \\ 0 & V_{\text{sky}} \end{bmatrix} \end{aligned} \tag{17}$$

where j_+^A and j_-^A are the upward and downward atmospheric thermal radiation fluxes, respectively. j_o^A is the atmospheric flux-equivalent thermal radiance in the view direction (i.e., the path thermal radiance of the atmosphere times π). j_+^L is the surface upward thermal radiation flux, and j_o^L is the surface flux-equivalent thermal radiance in the view direction. J_+^A is the upward radiation flux to which the thermal radiation contributes (i.e., without solar contribution) at the TOA, and J_o^A is the flux-equivalent radiance to which the thermal radiation contributes in the view direction

$$\begin{aligned} J_o^A = {} & j_o^A + \tau_{oo}^A J_o^L \zeta + \frac{\tau_{do}^A V_{\text{sky}} \left(j_+^L + r_{dd}^L V_{\text{sky}} j_-^A\right)}{1 - r_{dd}^L \rho_{dd}^{A\_b}} \\ & + \frac{\tau_{oo}^A r_{do}^L \left(V_{\text{sky}} j_-^A + \rho_{dd}^{A\_b} j_+^L\right)}{1 - r_{dd}^L \rho_{dd}^{A\_b}} \end{aligned} \tag{18}$$

$$J_+^A = j_+^A + \frac{\tau_{dd}^A V_{\text{sky}} \left(j_+^L + r_{dd}^L V_{\text{sky}} j_-^A\right)}{1 - r_{dd}^L \rho_{dd}^{A\_b}}. \tag{19}$$

Therefore, the TOA directional radiance L_o^A for a sloping surface is expressed as

$$L_o^A = \left(E_s^A \cos\theta_s r_{so}^A + J_o^A\right)/\pi \tag{20}$$

and the TOA upward radiation (E_+^A) and TOA net radiation (E_{net}^A) are

$$E_+^A = E_s^A \cos\theta_s r_{sd}^A + J_+^A \tag{21}$$

$$E_{\text{net}}^A = E_s^A - E_+^A. \tag{22}$$

The detailed modeling process is given in Appendix A. This RTM-CF is highly modularized and is suitable for different surfaces, such as soil and snow, as only the surface reflectance matrix R_s^L is accurately modeled. However, it should be noted that their extra caution is required for vegetated terrain surfaces. Due to the influence of gravitropism, leaves grow against the direction of gravity instead of in the direction of the surface normal. Therefore, the influence of gravitropism on the leaf angle distribution (LAD) and R_s^L needs to be considered. An algorithm for modeling the geotropic effects on the LAD was proposed and published in [53], and the technical details of that process are not repeated here for the sake of retaining clarity. In this study, the proposed RTM-CF considers the influence of gravitropism on vegetated surfaces.

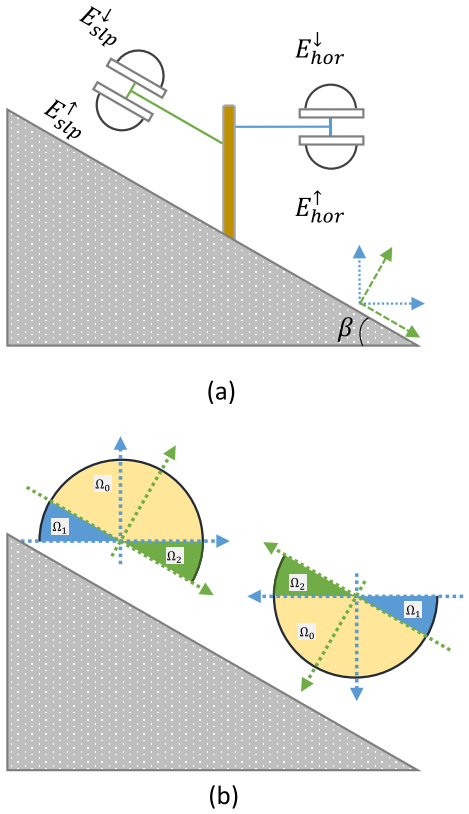

Fig. 2. Schematic for the radiation that refers to the sloping (in green) and horizontal (in blue) coordinates. The inclined angle is β. (a) Two slope-parallel positioned radiometers measure surface downward ($E_{\text{slp}}^{\downarrow}$) and upward ($E_{\text{slp}}^{\uparrow}$) radiations that refer to the sloping surface, and the two horizontal radiometers measure surface downward ($E_{\text{hor}}^{\downarrow}$) and upward ($E_{\text{hor}}^{\uparrow}$) radiations that refer to the horizontal plane. (b) Radiative flux components of slope-parallel and horizontal radiometers. Radiance in the direction of Ω_0 and Ω_2 contributes to $E_{\text{slp}}^{\downarrow}$ and $E_{\text{slp}}^{\uparrow}$, while radiance in the direction of Ω_0 and Ω_1 contributes to $E_{\text{hor}}^{\downarrow}$ and $E_{\text{hor}}^{\uparrow}$. Usually, the proximal sensors are installed horizontally in the field. (For the interpretation of the references to different colors in the legend of this figure, the reader is referred to the web version of this article.)

2) Modeling of the Surface Parameters: The surface radiation fluxes on a horizontal plane and a sloping surface are different. The differences between them are described first before the equations of surface parameters are given, and Fig. 2(a) shows a schematic to illustrate them. Methods for modeling the two kinds of radiation parameters are given in this study: parameters with the slp subscript refer to the sloping coordinate, whereas parameters with the hor subscript refer to the horizontal coordinate. The basic principles are illustrated in Fig. 2(b). The radiance in the direction of Ω_0 and Ω_2 contributes to the downward radiation ($E_{\text{slp}}^{\downarrow}$) and the upward radiation ($E_{\text{slp}}^{\uparrow}$) that refer to the sloping surface, while the radiance in the direction of Ω_0 and Ω_1 contributes to the downward radiation ($E_{\text{hor}}^{\downarrow}$) and upward radiation ($E_{\text{hor}}^{\uparrow}$) that refer to the horizontal plane. A step-by-step derivation is given in Appendix A.

Surface downward radiation on the slope is the sum of the incident surface solar radiation ($\mathrm{SSR}^{\downarrow}_{\mathrm{slp}}$) and downward surface thermal radiation ($\mathrm{STR}^{\downarrow}_{\mathrm{slp}}$)

$$E^{\downarrow}_{\mathrm{slp}} = \int_{\lambda_1}^{\lambda_2} \left(\mathrm{SSR}^{\downarrow}_{\mathrm{slp}} + \mathrm{STR}^{\downarrow}_{\mathrm{slp}}\right) d\lambda \tag{23}$$

where

$$\mathrm{SSR}^{\downarrow}_{\mathrm{slp}} = P_{11}\left(I - R^A_b R^L_s\right)^{-1} P^{in}_T T^A_d E^A_d \tag{24}$$

$$\mathrm{STR}^{\downarrow}_{\mathrm{slp}} = P_{01}\left(I - R^A_b J^L_s\right)^{-1} Q_T J^A_d. \tag{25}$$

Particularly, the PAR and ISR are $E^{\downarrow}_{\mathrm{slp}}$ in the spectral ranges of 400–700 and 300–3000 nm, respectively, i.e., the integration of $\mathrm{SSR}^{\downarrow}_{\mathrm{slp}}$ over the spectrum.

Similarly, surface upward radiation ($E^{\uparrow}_{\mathrm{slp}}$) from the sloping surface is given as

$$E^{\uparrow}_{\mathrm{slp}} = \int_{\lambda_1}^{\lambda_2} \left(\mathrm{SSR}^{\uparrow}_{\mathrm{slp}} + \mathrm{STR}^{\uparrow}_{\mathrm{slp}}\right) d\lambda \tag{26}$$

$$\mathrm{SSR}^{\uparrow}_{\mathrm{slp}} = P_{10} R^L_s \left(I - R^A_b R^L_s\right)^{-1} P^{in}_T T^A_d E^A_d \tag{27}$$

$$\mathrm{STR}^{\uparrow}_{\mathrm{slp}} = P_{10} J^L_s \left(I - R^A_b J^L_s\right)^{-1} Q_T J^A_d. \tag{28}$$

The corresponding downward surface radiation on the horizontal plane can be expressed as

$$E^{\downarrow}_{\mathrm{hor}} = \int_{\lambda_1}^{\lambda_2} \left(\mathrm{SSR}^{\downarrow}_{\mathrm{hor}} + \mathrm{STR}^{\downarrow}_{\mathrm{hor}}\right) d\lambda \tag{29}$$

$$\mathrm{SSR}^{\downarrow}_{\mathrm{hor}} = P_{11} H_T \left(I - R^A_b R^L_s\right)^{-1} P^{in}_T T^A_d E^A_d \tag{30}$$

$$\mathrm{STR}^{\downarrow}_{\mathrm{hor}} = P_{01} Q_T \left(I - R^A_b J^L_s\right)^{-1} Q_T J^A_d. \tag{31}$$

and the upward surface radiation from the horizontal plane is

$$E^{\uparrow}_{\mathrm{hor}} = \int_{\lambda_1}^{\lambda_2} \left(\mathrm{SSR}^{\uparrow}_{\mathrm{hor}} + \mathrm{STR}^{\uparrow}_{\mathrm{hor}}\right) d\lambda \tag{32}$$

$$\mathrm{SSR}^{\uparrow}_{\mathrm{hor}} = P_{10} P^{\mathrm{out}}_T R^L_s \left(I - R^A_b R^L_s\right)^{-1} P^{in}_T T^A_d E^A_d \tag{33}$$

$$\mathrm{STR}^{\uparrow}_{\mathrm{hor}} = P_{10} P^{\mathrm{out}}_T J^L_s \left(I - R^A_b J^L_s\right)^{-1} Q_T J^A_d \tag{34}$$

where

$$H_T = \begin{bmatrix} H_{\mathrm{sun}} & 0 \\ 0 & V_{\mathrm{sky}} \end{bmatrix}; \quad H_{\mathrm{sun}} = \zeta \frac{\cos\theta_s}{\cos\theta_{is}} \tag{35}$$

$P_{11} = [1, 1]$, $P_{10} = [1, 0]$, and $P_{01} = [0, 1]$ are extraction matrices. In particular, SNR can be calculated by

$$E^L_{\mathrm{net}} = E^{\downarrow}_{\mathrm{hor}} - E^{\uparrow}_{\mathrm{hor}}. \tag{36}$$

The surface albedo is the ratio of the reflected and incident radiation. Its equation for the sloping surface is

$$\mathrm{Albedo}_{\mathrm{slp}} = \frac{\int_{\lambda_1}^{\lambda_2} \mathrm{SSR}^{\uparrow}_{\mathrm{slp}} d\lambda}{\int_{\lambda_1}^{\lambda_2} \mathrm{SSR}^{\downarrow}_{\mathrm{slp}} d\lambda} \tag{37}$$

and its equation for the horizontal plane is given as

$$\mathrm{Albedo}_{\mathrm{hor}} = \frac{\int_{\lambda_1}^{\lambda_2} \mathrm{SSR}^{\uparrow}_{\mathrm{hor}} d\lambda}{\int_{\lambda_1}^{\lambda_2} \mathrm{SSR}^{\downarrow}_{\mathrm{hor}} d\lambda}. \tag{38}$$

For the visible albedo, λ_1 and λ_2 are 400 and 700 nm, respectively, whereas they are 300 and 3000 nm for the short-wave albedo.

The absorbed photosynthetically active radiation (APAR) is the portion of the PAR absorbed by vegetation, and the FAPAR is their ratio, i.e., FAPAR = APAR/PAR. If the land surface is covered by vegetation, then the APAR is

$$\mathrm{APAR} = \int_{400}^{700} \left[\left(P_{11} - P_{10} R^L_s\right) - \left(P_{11} - P_{10} R^s_s\right) \tilde{D}^v\right] \times \left(I - R^A_b R^L_s\right)^{-1} P^{in}_T T^A_d E^A_d d\lambda \tag{39}$$

where $\tilde{D}^v = (I - R^v_b R^s_s)^{-1} T^v_d$ is the equivalent transmittance matrix (the superscript "v" represents the canopy) for the canopy [47], and R^s_s is the reflectance matrix of soil. It is critical that the FAPAR value is different if different coordinates ($\mathrm{PAR}_{\mathrm{slp}}$ or $\mathrm{PAR}_{\mathrm{hor}}$) are taken as a reference. The value calculated by $\mathrm{FAPAR} = \mathrm{APAR}/\mathrm{PAR}_{\mathrm{slp}}$ is used in this study.

The surface BRF is also different when different coordinates are used, and their relationship is

$$\mathrm{BRF}_{\mathrm{hor}} = \mathrm{BRF}_{\mathrm{slp}} \cdot F_{\mathrm{sun}}. \tag{40}$$

B. Validation Scheme

Four VS are implemented to test the performance of the proposed optical–thermal RTM-CF with topographic effects. The first three schemes are achieved through comparison with the well-known 3-D ray-tracing model DART [13], [54], which has been recognized as a benchmark RTM [12]. For the submodels of the RTM-CF, the atmospheric variables simulated by the MODTRAN model are used, and the surface variables are simulated by the 4SAILT canopy RTM [53]. In 4SAILT, the influences of gravitropism on R^L_s are modeled.

1) VS-1: The first VS (VS-1) focuses on the TOA directional radiance, which corresponds to satellite observations. The TOA directional radiance [i.e., (20)] at the center bands of Landsat-8 (0.44, 0.48, 0.56, 0.65, 0.87, 1.61, 2.2, 11.1, and 12.0 μm) is simulated and validated.

2) VS-2: The second VS (VS-2) focuses on surface radiation. Surface downward, upward, and net radiation fluxes are simulated and validated. The simulations are conducted at 10-nm intervals between 0.35 and 2.5 μm, 50-nm intervals for 2.5–5.5 μm, and 100-nm intervals for 5.5–15.0 μm.

3) VS-3: The third VS (VS-3) focuses on the short-wave spectrum, and thermal contributions are neglected. Twelve parameters are validated: 1) the TOA reflectance; 2) the surface BRF that corresponds to situations in which the incident radiation only contains direct irradiance; 3) the surface HDRF that corresponds to situations in which the incident radiation only contains diffuse irradiance; 4) the surface reflectance, in which the results, essentially weighted by the BRF and HDRF, under different atmospheric conditions are evaluated; 5) the APAR; 6) the FAPAR; 7) the $\mathrm{PAR}_{\mathrm{slp}}$; 8) the $\mathrm{PAR}_{\mathrm{hor}}$; 9) the $\mathrm{ISR}_{\mathrm{slp}}$; 10) the short-wave $\mathrm{albedo}_{\mathrm{slp}}$; 11) the $\mathrm{ISR}_{\mathrm{hor}}$; and 12) the short-wave $\mathrm{albedo}_{\mathrm{hor}}$. The first four parameters are simulated at the center bands of Landsat-8 (0.44, 0.48, 0.56, 0.65, 0.87, 1.61, and 2.2 μm).

Table II gives the configurations of the models for comparison under VS-1–VS-3. Three atmospheric conditions are predefined: a molecular atmosphere, an aerosol atmosphere, and a cloudy atmosphere. A gentle slope (10°) and a steep

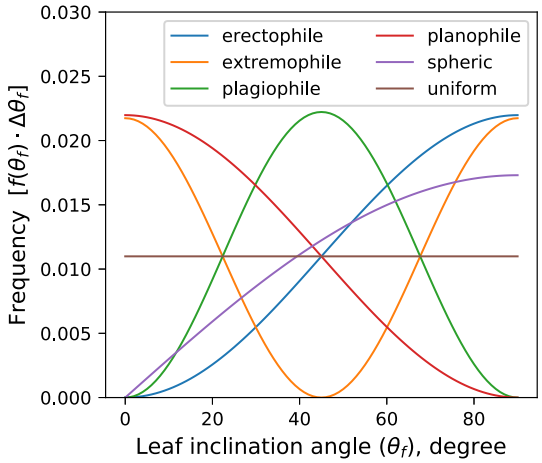

Fig. 3. Six typical LAD functions: uniform, spheric, erectophile, planophile, extremophile, and plagiophile. θ_f is the leaf inclination angle. $f(\theta_f)$ is the leaf inclination density function, and $\int_0^{2\pi} f(\theta_f)d\theta_f = 1$. (For the interpretation of the references to different colors in the legend of this figure, the reader is referred to the web version of this article.)

slope (40°) are configured. The solar and view zenith angles that refer to the horizontal plane range from 0° to 40°, and thus, the corresponding zenith angle that refers to the slope spans from 0° to 80°. For VS-1 and VS-2, the leaf and soil spectra (0.35–15.0 μm) used in [53] are adopted in this study. For VS-3, various biophysical and biochemical canopy conditions are simulated by the PROSPECT model, and two soil reflectance spectra (one high-reflectivity spectrum and one low-reflectivity spectrum) are used to incorporate more situations. Six typical LAD functions are used in this study, which is plotted in Fig. 3, and modeling the influences of gravitropism on LAD can be found in the 4SAILT model [53].

4) VS-4: The fourth VS (VS-4) uses field measurements. Diurnal observations from three field sites are used to validate the model. Information about the three sites is given in Table III. The DYK site is located in the Qilian Mountains of northwest China, where two horizontal and two sloping CNR4 radiometers are installed [55]. The ESM and ESR sites are located in the Riviera Valley in southern Switzerland, where two CM21 (CM11) radiometers are set horizontally, and two CNR1 radiometers are slope-parallel installed [56]. For each site, the diurnal downwelling and upwelling irradiances that refer to both the slope and the horizontal plane [see Fig. 2(a)] are observed; thus, the corresponding albedo can be calculated. More details about the three sites can be found in [55] and [56]. Due to the lack of measurements of the necessary atmospheric and surface parameters, the atmospheric conditions are assumed to be clear in the simulation, and we try to fit the observations to obtain suitable inputs. For the same reason, it is difficult to compare the simulated and observed results directly. Therefore, the ratio of the horizon parameter to the corresponding slope parameter is used as a bridge, and its correlation is checked because this ratio is independent of the optical and structural parameters to some degree [55].

TABLE II

SETTING OF THE PARAMETERS FOR THE COMPARISON OF THE DART MODEL AND THE PROPOSED MODEL. LAD: LEAF ANGLE DISTRIBUTION

Parameter	Values	Units
Atmosphere	molecular atmosphere aerosol atmosphere cloud atmosphere	-
Solar zenith angle	5, 15, 25, 35	degrees
Solar azimuth angle	0	degrees
View zenith angle	0, 10, 20, 30, 40	degrees
View azimuth angle	0, 90, 180, 270	degrees
Slope	10, 40	degrees
Aspect	0, 90, 180	degrees
Leaf area index	1, 3, 6	m^2/m^2
LAD	uniform, spheric, erectophile, planophile, extremophile, plagiophile	-
Leaf chlorophyll	30, 80	$\mu g/cm^2$
Leaf water	0.02	cm
Leaf dry matter	0.005, 0.015	g/cm^2
Soil spectrum	low, high [reflectivity]	-
Leaf temperature	10, 30	°C
Soil temperature	10, 30	°C

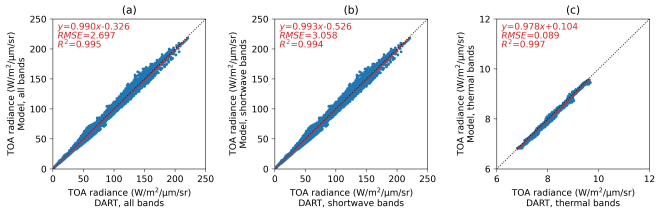

Fig. 4. Comparison of the simulated TOA radiance at the center bands of Landsat-8 (0.44, 0.48, 0.56, 0.65, 0.87, 1.61, 2.2, 11.1, and 12.0 μm) with the DART. (a) Comparison of all nine bands. (b) Results for the short-wave bands (0.44, 0.48, 0.56, 0.65, 0.87, 1.61, and 2.2 μm). (c) Results for the thermal bands (11.1 and 12.0 μm).

III. RESULTS AND ANALYSES

A. Validation With the 3-D DART Model

1) VS-1: The comparisons of TOA radiance are shown in Fig. 4. Fig. 4(a) and (b) shows the results for all bands and the short-wave bands, respectively, while Fig. 4(c) shows the results for the thermal bands. The coupled surface–atmosphere RTM achieves great consistency with the DART, with an overall RMSE < 3 W/m^2/μm/sr and $R^2 > 0.99$.

2) VS-2: The results for the second VS are shown in Fig. 5. Surface downward, upward, and net radiation fluxes at the horizontal plane are evaluated at different spectral ranges: 1) 0.35–15 μm; 2) an optical range of 0.35–3 μm; and 3) a thermal range of 3–15 μm. The 12 subplots of Fig. 5 show that the simulated surface radiation fluxes agree with the DART results, with a high R^2 (>0.97), low RMSE, and scatter points close to the 1:1 lines. This demonstrates that the proposed unified optical–thermal RTM-CF with topographic effects is accurate for surface radiation calculations. There are some clustered points in the scatter plots because the

TABLE III

INFORMATION ABOUT THE THREE FIELD SITES FOR EVALUATING THE FORWARD MODEL (FROM [55]). FOR EACH SITE, THE DIURNAL DOWNWARD AND UPWARD IRRADIANCES ARE MEASURED

Latitude (°)	Longitude (°)	Site name	Elevation (m)	Slope (°)	Aspect (°)	Surface type	Date	Atmospheric condition
38.57	100.23	DYK	2884	36	247	Grassland	2016.09.14	Clear
46.27	9.04	ESM	1060	20	236	Alpine	1999.08.25	Clear, cloudy
46.27	9.06	ESR	2110	40	242	Alpine meadow	1999.09.14	Clear, cloudy

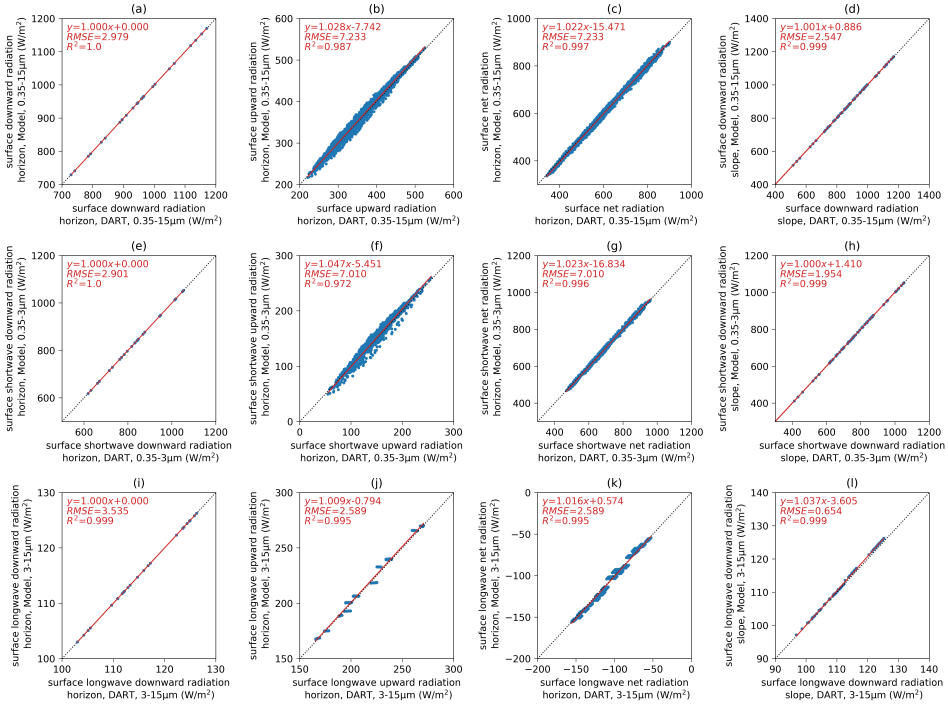

Fig. 5. Comparison of the surface radiation fluxes with the DART under different atmospheric and land surface characterizations. The first column contains the surface downward radiation at the horizontal plane: (a) 0.35–15 μm, (e) 0.35–3 μm, and (i) 3–15 μm. The second column contains the surface upward radiation at the horizontal plane: (b) 0.35–15 μm, (f) 0.35–3 μm, and (j) 3–15 μm. The third column contains the SNR at the horizontal plane: (c) 0.35–15 μm, (g) 0.35–3 μm, and (k) 3–15 μm. The fourth column contains the surface downward radiation on the sloping surface: (d) 0.35–15 μm, (h) 0.35–3 μm, and (l) 3–15 μm. Configurations of the parameters are given in Table II.

downward radiation is mainly controlled by atmospheric conditions, the solar position, the slope, and the aspect; and the surface-emitted radiation is mainly controlled by the leaf temperature, the soil temperature, and the slope.

3) VS-3: Comparisons with the DART model for the short-wave range are shown in Fig. 6. Fig. 6(a) shows that the simulated TOA reflectance values are in good agreement with the DART results. The simulated downward solar radiation (both on the horizontal plane and on the slope) matches perfectly with the DART results ($R^2 > 0.99$), as shown in Fig. 6(g)–(i) and (k). The simulated surface BRF, HDRF, and reflectance are consistent with the DART results, with all $R^2 > 0.99$ and RMSE < 0.01. Both the simulated surface short-wave albedos that refer to the horizontal plane and to the slope fit well with the DART values, with RMSE values of approximately 0.01, as shown in Fig. 6(j) and (l). Compared with the DART-based APAR, the simulated APAR has an RMSE of 8.5 W/m^2, with $R^2 > 0.99$, and the corresponding FAPAR has an RMSE of 0.033, with $R^2 > 0.98$.

In general, the simulated results obtained by the coupled surface–atmosphere model are consistent with the DART results. The discrepancies shown are mainly from the different processes of radiative transfer through the canopy—DART is a 3-D model with many vegetation voxels, while the proposed model is a 1-D model with homogeneous scenes.

In addition, for the situation where the topographic effect is not considered, the comparisons of the simulation results and those obtained with DART using the same parameters for VS-1–VS-3 are given in Figs. S1–S3 in the Supplementary Material. This demonstrates that ignoring topographic effects can lead to significant errors in both the TOA-level and BOA-level parameters.

B. Validation by Field Measurement (VS-4)

The evaluations with the data from the DYK, ESM, and ESR sites are shown in Fig. 7. The diurnal changes in the downward radiation that refer to both the horizontal plane and the slope are in the first row, while the diurnal changes in the albedo are in the third row. The changes in the atmospheric conditions can also be observed from the diurnal observations from all three sites, especially at the ESR site, where cloud influences are obvious. Although the simulated results are assumed to have been obtained under clear atmospheric conditions, it can still

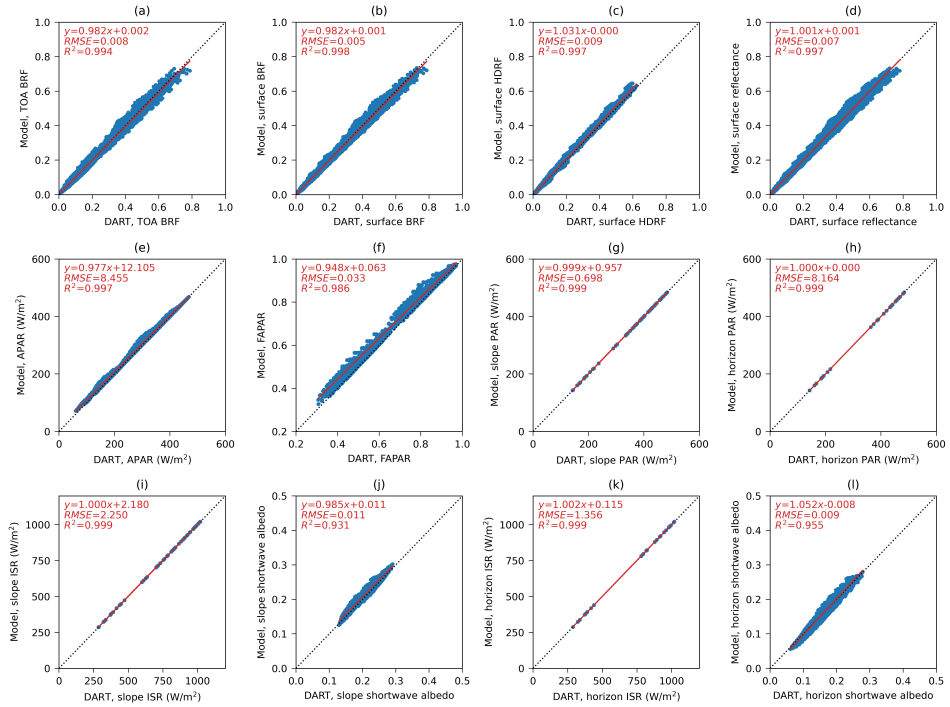

Fig. 6. Comparison of the proposed model with the DART under different atmospheric and land surface characterizations. (a) TOA reflectance at the center bands of Landsat-8. (b) Surface BRF at the center bands of Landsat-8. (c) Surface HDRF at the center bands of Landsat-8. (d) Surface reflectance at the center bands of Landsat-8. (e) APAR, in W/m^2. (f) FAPAR. (g) PAR_{slp}, in W/m^2. (h) PAR_{hor}, in W/m^2. (i) ISR_{slp}, in W/m^2. (j) short-wave $\text{albedo}_{\text{slp}}$. (k) ISR_{hor}, in W/m^2. (l) short-wave $\text{albedo}_{\text{hor}}$. Configurations of the parameters are given in Table II.

be seen that the proposed model captures the diurnal changes in the ISR and albedo well, with the absolute values displaying some discrepancies. The scatter plots of the simulated and measured $\text{ISR}_{\text{hor}}/\text{ISR}_{\text{slp}}$ values are shown in the second row of Fig. 7, while the comparison of the $\text{Albedo}_{\text{hor}}/\text{Albedo}_{\text{slp}}$ values is in the last row. The simulated ratios have good correlations with the measured ratios, and $R^2 > 0.96$. Overall, the proposed model performs very well with the selected field sites.

IV. Discussion

Although the validation results demonstrate that the proposed surface–atmosphere RTM-CF is accurate, several issues still need to be addressed or at least considered to improve the model in the future.

A. 3-D Effect of Clouds

The proposed model is based on the four-stream theory, which is a layer-stack modeling method. Like many algorithms that estimate surface radiation parameters through 1-D models, the proposed model also cannot handle the 3-D effect of clouds [57], [58]. Ideally, the atmosphere layer can be "replaced" by a complex 3-D atmospheric RTM, from which the 3-D effect of clouds can be incorporated and from which the atmospheric transmittance and reflectance variables are simulated. However, this would make the model too complex to be used in practice, such as in situations with parameter inversion. Therefore, the 1-D model scheme is adopted for now.

B. Efficiency

Efficiency is another issue. This model coupling framework runs fast because the radiative transfer processes are efficiently modeled. However, atmospheric RTMs, such as MODTRAN, are time-consuming. One possible solution is to use lookup table techniques [47], [59]. In addition, our recent study on using machine learning techniques to accelerate RTMs [60] provided a potential solution. The coupled surface–atmosphere model could be replaced by a Gaussian process regression emulator, thereby achieving acceleration. More technical details are given in the work of Shi *et al.* [60].

C. Composite Slope and Terrain Irradiance

This study is built on the assumption of a solo sloping surface, which is reasonable for high spatial resolution data. Nevertheless, it is not clear if this assumption is valid for moderate spatial resolution data, such as the 500-m MODIS observations, because of the mutual offset effects within large pixels. It is also not easy to quantify the discrepancies in this assumption because the variety of scenes within one 500-m pixel can be abundant. Possible solutions may be obtained from studies on the composite slope [27], [31], [61] or by finding a way to obtain an equivalent solo slope for a specific area.

Accordingly, the terrain irradiance from and to other pixels is neglected in the current work, but it is usually modeled for a composite slope scene. This assumption is acceptable for most situations, but it should be noted that it might lead to

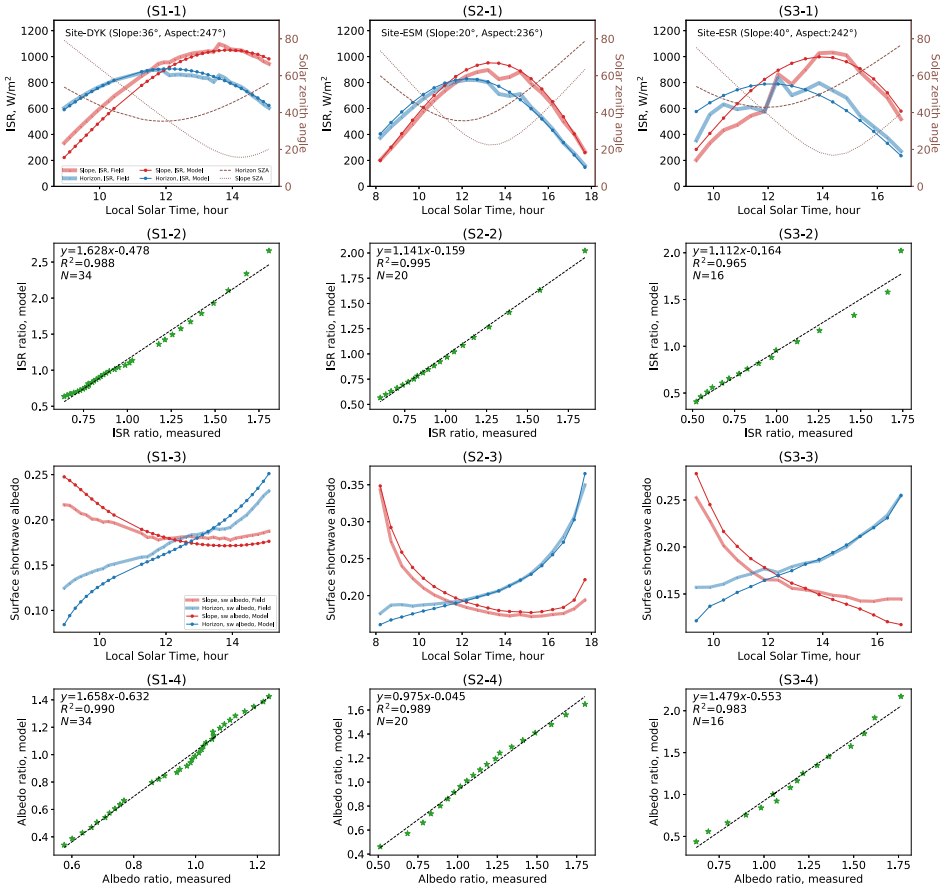

Fig. 7. Evaluation of the proposed model over three field sites with both horizontal and sloping sensors [see Fig. 2(a)]. S1: the DYK site. S2: the ESR site. S3: the ESM site. The first row contains the comparisons of field-measured and simulated ISR, in W/m^2. The second row is the scatter for the field-measured and simulated ISR ratios, which is the ratio of $\mathrm{ISR_{hor}}/\mathrm{ISR_{slp}}$. The third row contains the comparisons of field-measured and simulated short-wave albedos. The fourth row is the scatter for the field-measured and simulated albedo ratio, which is the ratio of $\mathrm{Albedo_{hor}}/\mathrm{Albedo_{slp}}$. (For an interpretation of the references to different colors in the legend of this figure, the reader is referred to the web version of this article.)

significant errors in mountainous areas with deep valleys or highly reflective areas (such as areas with fine snow) [62]. In addition, the computational efficiency of determining the terrain irradiance is also a problem to be solved, which, otherwise, hinders its practical use.

V. Conclusion

A unified optical–thermal surface–atmosphere RTM-CF with topographic effects is developed. The evaluation of the proposed framework with the 3-D ray-tracing model DART and over three field-measured observations shows that the framework achieves very good performance. Besides, this framework efficiently models radiative transfer processes, and it is much faster than DART because DART needs to trace lots of rays in many voxels to get accurate results.

Three advantages of the RTM-CF are given as follows.

1) Atmospheric and topographic effects are simultaneously coupled and considered at the BOA level, thus avoiding the complex atmospheric and topographic corrections normally required for the satellite observations. In addition, the anisotropic property of the surface can be effectively accounted for.
2) By coupling the surface and atmosphere RTMs, many surface parameters (e.g., the PAR, ISR, APAR, albedo, and SNR) can be estimated from the same physical model, which ensures the physical connections among them. This physical consistency among parameters is important to end-users who intend to use remote sensing parameter products and climate models to study global or regional climate change.
3) The framework has excellent modularity, which implies that it can be easily modified and extended. For example, researchers who are interested in aquatic studies can easily replace the surface model with a water RTM.

Future studies will focus on incorporating machine learning acceleration techniques into the model and introducing a scheme for composite slopes. In addition, the applicability of this model will be tested on high spatial resolution observations, such as Landsat-8 and Sentinel-2.

Appendix A
Four-Stream Theory-Based Modeling

A. Modeling of Solar Radiation Over Flat Surfaces

Assuming a homogeneous underlying surface, the modeling of the TOA reflectance over flat surfaces [15], [19], [23] is first introduced. As shown in Fig. 8, only direct solar irradiance $E_s(t)$ is assumed to exist at the TOA, and $E_o(t)$ is equals

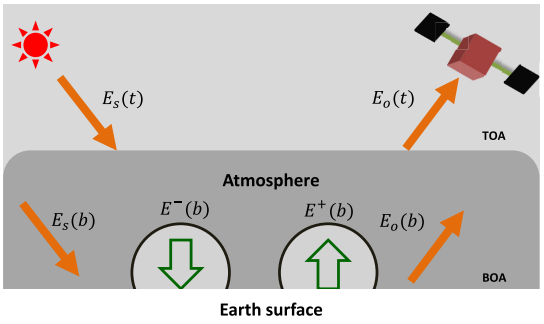

Fig. 8. Four-stream theory-based radiation fluxes over a flat surface at the TOA and BOA (after [19] and [34]).

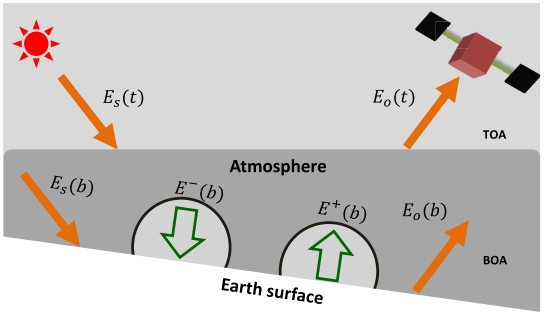

Fig. 9. Four-stream theory-based radiation fluxes over a slope at the TOA and BOA (after [19] and [34]).

to π times the radiance observed by the sensor. At the BOA, four fluxes are modeled: the attenuated direct solar flux $E_s(b)$, the diffuse downward flux $E^-(b)$, the diffuse upward flux $E^+(b)$, and the surface radiance (times π) in the view direction $E_o(b)$ [19], [34].

Equation (41) can be built based on the four-stream theory [15], [19], [34]

$$E_o(t) = \rho_{so}^A E_s(t) + \tau_{do}^A E^+(b) + \tau_{oo}^A E_o(b) \quad (41a)$$
$$E_o(b) = r_{so}^L E_s(b) + r_{do}^L E^-(b) \quad (41b)$$
$$E^+(b) = r_{sd}^L E_s(b) + r_{dd}^L E^-(b) \quad (41c)$$
$$E^-(b) = \tau_{sd}^A E_s(t) + \rho_{dd}^{A\_b} E^+(b) \quad (41d)$$
$$E_s(b) = \tau_{ss}^A E_s(t) \quad (41e)$$

where the physical meaning of the reflectance and transmittance variables is given in Table I.

By solving (41)

$$E_o(t) = \left\{ \rho_{so}^A + \tau_{ss}^A r_{so}^L \tau_{oo}^A + \frac{\left(\tau_{ss}^A r_{sd}^L + \tau_{sd}^A r_{dd}^L\right)\tau_{do}^A}{1 - r_{dd}^L \rho_{dd}^{A\_b}} + \frac{\left(\tau_{sd}^A + \tau_{ss}^A r_{sd}^L \rho_{dd}^{A\_b}\right) r_{do}^L \tau_{oo}^A}{1 - r_{dd}^L \rho_{dd}^{A\_b}} \right\} E_s(t) \quad (42a)$$

$$E_o(b) = \left\{ \tau_{ss}^A r_{so}^L + \frac{\left(\tau_{sd}^A + \tau_{ss}^A r_{sd}^L \rho_{dd}^{A\_b}\right) r_{do}^L}{1 - r_{dd}^L \rho_{dd}^{A\_b}} \right\} E_s(t) \quad (42b)$$

$$E^+(b) = \frac{\left(\tau_{ss}^A r_{sd}^L + \tau_{sd}^A r_{dd}^L\right)}{1 - r_{dd}^L \rho_{dd}^{A\_b}} E_s(t) \quad (42c)$$

$$E^-(b) = \frac{\left(\tau_{sd}^A + \tau_{ss}^A r_{sd}^L \rho_{dd}^{A\_b}\right)}{1 - r_{dd}^L \rho_{dd}^{A\_b}} E_s(t) \quad (42d)$$

where $E_s(t) = E_s^A \cos(\theta_s)$ and the ratio of $E_o(t)$ to $E_s(t)$ is $\bar{r}_{so}^A$ [i.e., (4)]. (42b) gives the BOA radiance (times π) in the view direction. In addition, (41e) and (42d) provide the direct downward radiation and diffuse downward radiation, respectively, and their sum is the SSR. Equation (42c) gives the upward radiation, and it can be further used to calculate the surface albedo [20].

B. Modeling Over Sloping Surfaces and Considering Thermal Radiation

In this study, by modeling the atmosphere-surface interactions at the sloping surface and considering the contributions of thermal radiation, (41) changes to (43). The radiation fluxes are now referred to as the sloping surface, as shown in Fig. 9

$$E_o(t) = \rho_{so}^A E_s(t) + \tau_{do}^A V_{\text{sky}} E^+(b) + \tau_{oo}^A E_o(b) + j_o^A \quad (43a)$$
$$E_o(b) = r_{so}^L E_s(b) + r_{do}^L E^-(b) + j_o^L \quad (43b)$$
$$E^+(b) = r_{sd}^L E_s(b) + r_{dd}^L E^-(b) + j_+^L \quad (43c)$$
$$E^-(b) = F_{\text{sky}} \tau_{sd}^A E_s(t) + \rho_{dd}^{A\_b} E^+(b) + V_{\text{sky}} j_-^A \quad (43d)$$
$$E_s(b) = F_{\text{sun}} \tau_{ss}^A E_s(t). \quad (43e)$$

By solving (43)

$$\begin{aligned} E_o(t) = {} & \left(\rho_{so}^A + \tau_{oo}^A r_{so}^L F_{\text{sun}} \tau_{ss}^A\right) E_s(t) + j_o^A + \tau_{oo}^A J_o^L \\ & + \frac{\tau_{do}^A V_{\text{sky}} \left(r_{sd}^L F_{\text{sun}} \tau_{ss}^A + r_{dd}^L F_{\text{sky}} \tau_{sd}^A\right)}{1 - r_{dd}^L \rho_{dd}^{A\_b}} E_s(t) \\ & + \frac{\tau_{oo}^A r_{do}^L \left(F_{\text{sky}} \tau_{sd}^A + \rho_{dd}^{A\_b} r_{sd}^L F_{\text{sun}} \tau_{ss}^A\right)}{1 - r_{dd}^L \rho_{dd}^{A\_b}} E_s(t) \\ & + \frac{\tau_{do}^A V_{\text{sky}} \left(j_+^L + r_{dd}^L V_{\text{sky}} j_-^A\right)}{1 - r_{dd}^L \rho_{dd}^{A\_b}} \\ & + \frac{\tau_{oo}^A r_{do}^L \left(V_{\text{sky}} j_-^A + \rho_{dd}^{A\_b} j_+^L\right)}{1 - r_{dd}^L \rho_{dd}^{A\_b}} \end{aligned} \quad (44a)$$

$$\begin{aligned} E_o(b) = {} & \tau_{ss}^A r_{so}^L F_{\text{sun}} E_s(t) + j_o^L \\ & + \frac{r_{do}^L \left(F_{\text{sky}} \tau_{sd}^A + \rho_{dd}^{A\_b} r_{sd}^L F_{\text{sun}} \tau_{ss}^A\right)}{1 - r_{dd}^L \rho_{dd}^{A\_b}} E_s(t) \\ & + \frac{r_{do}^L \left(V_{\text{sky}} j_-^A + \rho_{dd}^{A\_b} j_+^L\right)}{1 - r_{dd}^L \rho_{dd}^{A\_b}} \end{aligned} \quad (44b)$$

$$\begin{aligned} E^+(b) = {} & \frac{\left(\tau_{ss}^A r_{sd}^L F_{\text{sun}} + \tau_{sd}^A r_{dd}^L F_{\text{sky}}\right)}{1 - r_{dd}^L \rho_{dd}^{A\_b}} E_s(t) \\ & + \frac{\left(j_+^L + r_{dd}^L V_{\text{sky}} j_-^A\right)}{1 - r_{dd}^L \rho_{dd}^{A\_b}} \end{aligned} \quad (44c)$$

$$\begin{aligned} E^-(b) = {} & \frac{\left(\tau_{sd}^A F_{\text{sky}} + \tau_{ss}^A r_{sd}^L \rho_{dd}^{A\_b} F_{\text{sun}}\right)}{1 - r_{dd}^L \rho_{dd}^{A\_b}} E_s(t) \\ & + \frac{\left(V_{\text{sky}} j_-^A + \rho_{dd}^{A\_b} j_+^L\right)}{1 - r_{dd}^L \rho_{dd}^{A\_b}}. \end{aligned} \quad (44d)$$

The ratio of $E_o(t)$ to $E_s(t)$ is r_{so}^A when ignoring the thermal contribution, which is the same as (11). $E^+(b)$ in (44c) and $E^-(b)$ in (44d) refer to the slope coordinate. $E^+(b)$ is the monochromatic radiation of $E_{\text{slp}}^{\uparrow}$ in Fig. 2, while $E^-(b)$ is the

diffuse part of $E^{\downarrow}_{\text{slp}}$

$$E^{\uparrow}_{\text{slp}} = \int_{\lambda_1}^{\lambda_2} E^{+}(b)d\lambda \tag{45}$$

$$E^{\downarrow}_{\text{slp}} = \int_{\lambda_1}^{\lambda_2} (E^{-}(b) + E_s(b))d\lambda \tag{46}$$

and their ratio is $\text{Albedo}_{\text{slp}}$ [i.e., (37)] if thermal radiation is ignored. For the upward and downward radiations that refer to the horizontal plane

$$E^{\uparrow}_{\text{hor}} = V_{\text{sky}} E^{\uparrow}_{\text{slp}} \tag{47}$$

$$E^{\downarrow}_{\text{hor}} = \int_{\lambda_1}^{\lambda_2} \left(\zeta \tau^{A}_{ss} E_s(t) + V_{\text{sky}} E_{-}(b)\right)d\lambda \tag{48}$$

and the ratio of $E^{\uparrow}_{\text{hor}}$ to $E^{\downarrow}_{\text{hor}}$ is $\text{Albedo}_{\text{hor}}$ if thermal radiation is ignored [i.e., (38)].

ACKNOWLEDGMENT

The authors would like to thank Dr. J.-P. Gastellu-Etchegorry for providing the DART Software. DART is distributed by Paul Sabatier University. It is freely available for research with public funding. A license of DART can be obtained by applying it at https://dart.omp.eu. The authors declare no conflict of interest.

REFERENCES

[1] F. Santini and A. Palombo, "Physically based approach for combined atmospheric and topographic corrections," *Remote Sens.*, vol. 11, no. 10, p. 1218, May 2019.

[2] S. Sandmeier and K. I. Itten, "A physically-based model to correct atmospheric and illumination effects in optical satellite data of rugged terrain," *IEEE Trans. Geosci. Remote Sens.*, vol. 35, no. 3, pp. 708–717, May 1997.

[3] R. Richter, "Correction of atmospheric and topographic effects for high spatial resolution satellite imagery," *Int. J. Remote Sens.*, vol. 18, no. 5, pp. 1099–1111, Mar. 1997.

[4] R. Richter, "Correction of satellite imagery over mountainous terrain," *Appl. Opt.*, vol. 37, no. 18, pp. 4004–4015, Jun. 1998.

[5] R. Richter and D. Schläpfer, "Geo-atmospheric processing of airborne imaging spectrometry data. Part 2: Atmospheric/topographic correction," *Int. J. Remote Sens.*, vol. 23, no. 13, pp. 2631–2649, Jan. 2002.

[6] J. D. Shepherd and J. R. Dymond, "Correcting satellite imagery for the variance of reflectance and illumination with topography," *Int. J. Remote Sens.*, vol. 24, no. 17, pp. 3503–3514, Jan. 2003.

[7] S. Kobayashi and K. Sanga-Ngoie, "The integrated radiometric correction of optical remote sensing imageries," *Int. J. Remote Sens.*, vol. 29, no. 20, pp. 5957–5985, Oct. 2008.

[8] L. Guanter, R. Richter, and H. Kaufmann, "On the application of the MODTRAN4 atmospheric radiative transfer code to optical remote sensing," *Int. J. Remote Sens.*, vol. 30, no. 6, pp. 1407–1424, Mar. 2009.

[9] J. Wen, Q. Liu, Q. Liu, Q. Xiao, and X. Li, "Parametrized BRDF for atmospheric and topographic correction and albedo estimation in Jiangxi rugged terrain, China," *Int. J. Remote Sens.*, vol. 30, no. 11, pp. 2875–2896, Jun. 2009.

[10] F. Li *et al.*, "A physics-based atmospheric and BRDF correction for landsat data over mountainous terrain," *Remote Sens. Environ.*, vol. 124, pp. 756–770, Sep. 2012.

[11] J. Wen *et al.*, "Modeling land surface reflectance coupled BRDF for HJ-1/CCD data of rugged terrain in Heihe river basin, China," *IEEE J. Sel. Topics Appl. Earth Observ. Remote Sens.*, vol. 8, no. 4, pp. 1506–1518, Apr. 2015.

[12] J.-P. Gastellu-Etchegorry *et al.*, "Discrete anisotropic radiative transfer (DART 5) for modeling airborne and satellite spectroradiometer and LIDAR acquisitions of natural and urban landscapes," *Remote Sens.*, vol. 7, no. 2, pp. 1667–1701, Feb. 2015.

[13] J.-P. Gastellu-Etchegorry *et al.*, "DART: Recent advances in remote sensing data modeling with atmosphere, polarization, and chlorophyll fluorescence," *IEEE J. Sel. Topics Appl. Earth Observ. Remote Sens.*, vol. 10, no. 6, pp. 2640–2649, Jun. 2017.

[14] J. Qi *et al.*, "LESS: LargE-scale remote sensing data and image simulation framework over heterogeneous 3D scenes," *Remote Sens. Environ.*, vol. 221, pp. 695–706, Feb. 2019.

[15] W. Verhoef, "Earth observation modeling based on layer scattering matrices," *Remote Sens. Environ.*, vol. 17, no. 2, pp. 165–178, Apr. 1985.

[16] E. F. Vermote, D. Tanre, J. L. Deuze, M. Herman, and J.-J. Morcette, "Second simulation of the satellite signal in the solar spectrum, 6S: An overview," *IEEE Trans. Geosci. Remote Sens.*, vol. 35, no. 3, pp. 675–686, May 1997.

[17] J. Qiu, "An improved model of surface BRDF-atmospheric coupled radiation," *IEEE Trans. Geosci. Remote Sens.*, vol. 39, no. 1, pp. 181–187, Jan. 2001.

[18] W. Qin, J. R. Herman, and Z. Ahmad, "A fast, accurate algorithm to account for non-Lambertian surface effects on TOA radiance," *J. Geophys. Res., Atmos.*, vol. 106, no. D19, pp. 22671–22684, Oct. 2001.

[19] W. Verhoef and H. Bach, "Simulation of hyperspectral and directional radiance images using coupled biophysical and atmospheric radiative transfer models," *Remote Sens. Environ.*, vol. 87, no. 1, pp. 23–41, Sep. 2003.

[20] W. Verhoef and H. Bach, "Coupled soil–leaf-canopy and atmosphere radiative transfer modeling to simulate hyperspectral multi-angular surface reflectance and TOA radiance data," *Remote Sens. Environ.*, vol. 109, no. 2, pp. 166–182, Jul. 2007.

[21] W. Verhoef and H. Bach, "Simulation of Sentinel-3 images by four-stream surface–atmosphere radiative transfer modeling in the optical and thermal domains," *Remote Sens. Environ.*, vol. 120, pp. 197–207, May 2012.

[22] B. Pinty *et al.*, "Coupling diffuse sky radiation and surface albedo," *J. Atmos. Sci.*, vol. 62, no. 7, pp. 2580–2591, Jul. 2005.

[23] W. Verhoef, L. Jia, Q. Xiao, and Z. Su, "Unified optical-thermal four-stream radiative transfer theory for homogeneous vegetation canopies," *IEEE Trans. Geosci. Remote Sens.*, vol. 45, no. 6, pp. 1808–1822, Jun. 2007.

[24] W. Verhoef, C. van der Tol, and E. M. Middleton, "Hyperspectral radiative transfer modeling to explore the combined retrieval of biophysical parameters and canopy fluorescence from FLEX–Sentinel-3 tandem mission multi-sensor data," *Remote Sens. Environ.*, vol. 204, pp. 942–963, Jan. 2018.

[25] H. Rahman, B. Pinty, and M. M. Verstraete, "Coupled surface-atmosphere reflectance (CSAR) model: 2. Semiempirical surface model usable with NOAA advanced very high resolution radiometer data," *J. Geophys. Res.*, vol. 98, no. D11, pp. 20791–20801, Nov. 1993.

[26] S. Liang and A. H. Strahler, "An analytic radiative transfer model for a coupled atmosphere and leaf canopy," *J. Geophys. Res., Atmos.*, vol. 100, no. D3, pp. 5085–5094, 1995.

[27] J. Wen *et al.*, "Characterizing land surface anisotropic reflectance over rugged terrain: A review of concepts and recent developments," *Remote Sens.*, vol. 10, no. 3, p. 370, Feb. 2018.

[28] Y. Chen, A. Hall, and K. N. Liou, "Application of three-dimensional solar radiative transfer to mountains," *J. Geophys. Res.*, vol. 111, no. D21, Nov. 2006, Art. no. D21111.

[29] W.-L. Lee, K. N. Liou, and A. Hall, "Parameterization of solar fluxes over mountain surfaces for application to climate models," *J. Geophys. Res.*, vol. 116, no. D1, Jan. 2011, Art. no. D01101.

[30] G. Yan, T. Wang, Z. Jiao, X. Mu, J. Zhao, and L. Chen, "Topographic radiation modeling and spatial scaling of clear-sky land surface longwave radiation over rugged terrain," *Remote Sens. Environ.*, vol. 172, pp. 15–27, Jan. 2016.

[31] Y. Wu, N. Wang, Z. Li, A. Chen, Z. Guo, and Y. Qie, "The effect of thermal radiation from surrounding terrain on glacier surface temperatures retrieved from remote sensing data: A case study from Qiyi Glacier, China," *Remote Sens. Environ.*, vol. 231, Sep. 2019, Art. no. 111267.

[32] G. Yan, Z.-H. Jiao, T. Wang, and X. Mu, "Modeling surface longwave radiation over high-relief terrain," *Remote Sens. Environ.*, vol. 237, Feb. 2020, Art. no. 111556.

[33] K. Wang, X. Zhou, J. Liu, and M. Sparrow, "Estimating surface solar radiation over complex terrain using moderate-resolution satellite sensor data," *Int. J. Remote Sens.*, vol. 26, no. 1, pp. 47–58, Jan. 2005.

[34] A. Mousivand, W. Verhoef, M. Menenti, and B. Gorte, "Modeling top of atmosphere radiance over heterogeneous non-Lambertian rugged terrain," *Remote Sens.*, vol. 7, no. 6, pp. 8019–8044, Jun. 2015.

[35] F. Gemmell, "An investigation of terrain effects on the inversion of a forest reflectance model," *Remote Sens. Environ.*, vol. 65, no. 2, pp. 155–169, Aug. 1998.
[36] A. Gonsamo and J. M. Chen, "Improved LAI algorithm implementation to MODIS data by incorporating background, topography, and foliage clumping information," *IEEE Trans. Geosci. Remote Sens.*, vol. 52, no. 2, pp. 1076–1088, Feb. 2014.
[37] S. Vanonckelen, S. Lhermitte, and A. Van Rompaey, "The effect of atmospheric and topographic correction methods on land cover classification accuracy," *Int. J. Appl. Earth Observ. Geoinf.*, vol. 24, pp. 9–21, Oct. 2013.
[38] B. Gao, L. Jia, and M. Menenti, "An improved method for retrieving land surface albedo over rugged terrain," *IEEE Geosci. Remote Sens. Lett.*, vol. 11, no. 2, pp. 554–558, Feb. 2014.
[39] P. Zhao, W. Fan, Y. Liu, X. Mu, X. Xu, and J. Peng, "Study of the remote sensing model of FAPAR over rugged terrains," *Remote Sens.*, vol. 8, no. 4, p. 309, Apr. 2016.
[40] A. Lipton, "Satellite-view biases in retrieved surface temperatures in mountain areas," *Remote Sens. Environ.*, vol. 60, no. 1, pp. 92–100, Apr. 1997.
[41] A. Loew *et al.*, "Do we (need to) care about canopy radiation schemes in DGVMs? Caveats and potential impacts," *Biogeosciences*, vol. 11, no. 7, pp. 1873–1897, Apr. 2014.
[42] M. Chernetskiy *et al.*, "Estimation of FAPAR over croplands using MISR data and the Earth observation land data assimilation system (EO-LDAS)," *Remote Sens.*, vol. 9, no. 7, p. 656, Jun. 2017.
[43] D. S. Boyd and F. Petitcolin, "Remote sensing of the terrestrial environment using middle infrared radiation (3.0–5.0 μm)," *Int. J. Remote Sens.*, vol. 25, no. 17, pp. 3343–3368, Sep. 2004.
[44] L. Giglio, W. Schroeder, and C. O. Justice, "The collection 6 MODIS active fire detection algorithm and fire products," *Remote Sens. Environ.*, vol. 178, pp. 31–41, Jun. 2016.
[45] D. Wang, S. Liang, T. He, and Q. Shi, "Estimating clear-sky all-wave net radiation from combined visible and shortwave infrared (VSWIR) and thermal infrared (TIR) remote sensing data," *Remote Sens. Environ.*, vol. 167, pp. 31–39, Sep. 2015.
[46] S. Liang, D. Wang, T. He, and Y. Yu, "Remote sensing of Earth's energy budget: Synthesis and review," *Int. J. Digit. Earth*, vol. 12, no. 7, pp. 737–780, Mar. 2019.
[47] H. Shi, Z. Xiao, S. Liang, and H. Ma, "A method for consistent estimation of multiple land surface parameters from MODIS top-of-atmosphere time series data," *IEEE Trans. Geosci. Remote Sens.*, vol. 55, no. 9, pp. 5158–5173, Sep. 2017.
[48] J. Dozier, J. Bruno, and P. Downey, "A faster solution to the horizon problem," *Comput. Geosci.*, vol. 7, no. 2, pp. 145–151, Jan. 1981.
[49] J. Dozier and J. Frew, "Rapid calculation of terrain parameters for radiation modeling from digital elevation data," *IEEE Trans. Geosci. Remote Sens.*, vol. 28, no. 5, pp. 963–969, Sep. 1990.
[50] J. E. Hay, "Calculating solar radiation for inclined surfaces: Practical approaches," *Renew. Energy*, vol. 3, nos. 4–5, pp. 373–380, Jun. 1993.
[51] Z.-H. Jiao, H. Ren, X. Mu, J. Zhao, T. Wang, and J. Dong, "Evaluation of four sky view factor algorithms using digital surface and elevation model data," *Earth Space Sci.*, vol. 6, no. 2, pp. 222–237, Feb. 2019.
[52] B. Y. H. Liu and R. C. Jordan, "The interrelationship and characteristic distribution of direct, diffuse and total solar radiation," *Sol. Energy*, vol. 4, no. 3, pp. 1–19, Jul. 1960.
[53] H. Shi and Z. Xiao, "The 4SAILT model: An improved 4SAIL canopy radiative transfer model for sloping terrain," *IEEE Trans. Geosci. Remote Sens.*, early access, Sep. 22, 2020, doi: 10.1109/TGRS.2020.3022874.
[54] E. Grau and J.-P. Gastellu-Etchegorry, "Radiative transfer modeling in the Earth–Atmosphere system with DART model," *Remote Sens. Environ.*, vol. 139, pp. 149–170, Dec. 2013.
[55] S. Wu *et al.*, "Characterization of remote sensing albedo over sloped surfaces based on DART simulations and *in situ* observations," *J. Geophys. Res., Atmos.*, vol. 123, no. 16, pp. 8599–8622, Aug. 2018.
[56] N. Matzinger, M. Andretta, E. van Gorsel, R. Vogt, A. Ohmura, and M. W. Rotach, "Surface radiation budget in an Alpine valley," *Quart. J. Roy. Meteorol. Soc.*, vol. 129, no. 588, pp. 877–895, Jan. 2003.
[57] K. Wyser, W. O'Hirok, C. Gautier, and C. Jones, "Remote sensing of surface solar irradiance with corrections for 3-D cloud effects," *Remote Sens. Environ.*, vol. 80, no. 2, pp. 272–284, May 2002.
[58] G. Huang *et al.*, "Estimating surface solar irradiance from satellites: Past, present, and future perspectives," *Remote Sens. Environ.*, vol. 233, Nov. 2019, Art. no. 111371.
[59] H. Shi, Z. Xiao, S. Liang, and X. Zhang, "Consistent estimation of multiple parameters from MODIS top of atmosphere reflectance data using a coupled soil-canopy-atmosphere radiative transfer model," *Remote Sens. Environ.*, vol. 184, pp. 40–57, Oct. 2016.
[60] H. Shi, Z. Xiao, and X. Tian, "Exploration of machine learning techniques in emulating a coupled soil–canopy–atmosphere radiative transfer model for multi-parameter estimation from satellite observations," *IEEE Trans. Geosci. Remote Sens.*, vol. 57, no. 11, pp. 8522–8533, Nov. 2019.
[61] D. Hao *et al.*, "Modeling anisotropic reflectance over composite sloping terrain," *IEEE Trans. Geosci. Remote Sens.*, vol. 56, no. 7, pp. 3903–3923, Jul. 2018.
[62] P. Sirguey, "Simple correction of multiple reflection effects in rugged terrain," *Int. J. Remote Sens.*, vol. 30, no. 4, pp. 1075–1081, Feb. 2009.

Hanyu Shi (Student Member, IEEE) received the B.S. and M.S. degrees from Beijing Normal University, Beijing, China, in 2014 and 2017, respectively, where he is pursuing the Ph.D. degree.

His research interests include radiative transfer and estimation of surface variables.

Zhiqiang Xiao (Member, IEEE) received the Ph.D. degree in geophysical prospecting and information technology from Central South University, Changsha, China, in 2004.

From 2004 to 2006, he was a Post-Doctoral Research Associate with Beijing Normal University, Beijing, China, where he is a Professor with the Faculty of Geographical Science. His research focuses on the retrieval of land biophysical parameters from remotely sensed data, assimilating radiometric observations into dynamic models.

Jianguang Wen (Member, IEEE) received the B.S. degree in geographic information systems and the M.S. degree in cartography and geographic information systems from Jilin University, China, in 2002 and 2005, respectively, and the Ph.D. degree in quantitative remote sensing from the Institute of Remote Sensing Applications, Chinese Academy of Sciences, Beijing, China, in 2008.

He has been a Professor with Aerospace Information Research Institute, Chinese Academy of Sciences, since 2011. His research focuses on modeling/inversion of land surface BRDF/albedo in rugged terrain from multiple remote sensing sensors. Field experiment techniques developed for land surface parameter validation is also a research interest.

Shengbiao Wu received the B.S. degree in base class of geography from Wuhan University, Wuhan, China, in 2013, and the Ph.D. degree from Aerospace Information Research Institute, Chinese Academy of Sciences, Beijing, China, in 2019.

He is a Post-Doctoral Fellow with the Faculty of Science, University of Hong Kong. His research mainly focused on the vegetation radiative transfer, surface biophysical parameter retrieval, land surface energy budget, and plant phenology diversity.